SCIENCE CHINA
Information Sciences

• **Supplementary File** •

The correlated matching decoder for the 4.8.8 color code

Yantong Liu[1], Junjie Wu[1*] & Lingling Lao[1*]

[1]*College of Computer Science and Technology, National University of Defense Technology, Changsha 410073, China*

Appendix A Mapping from surface code to color code

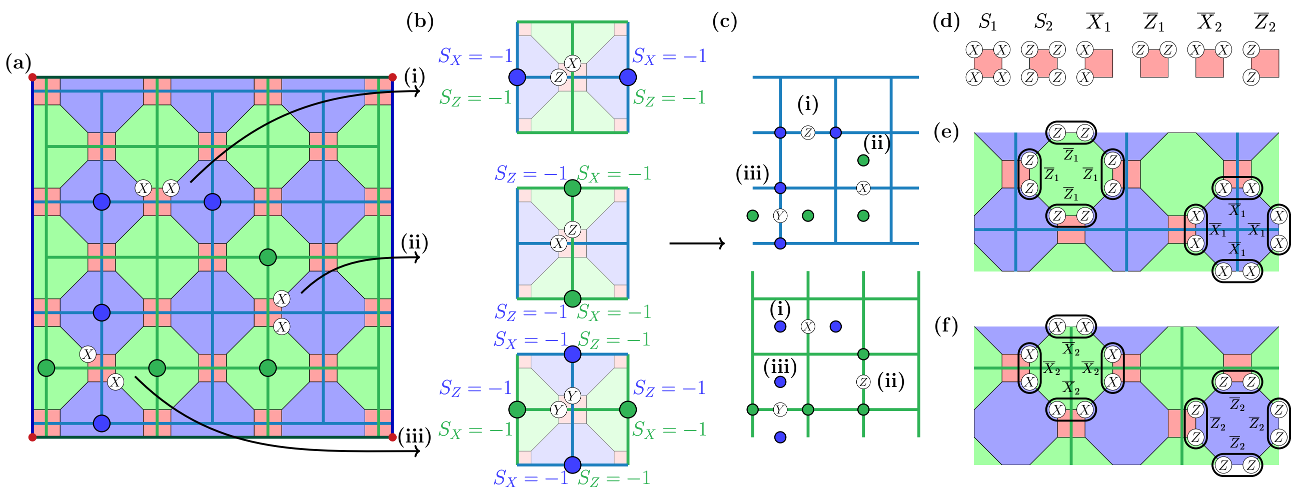

Figure A1 The surface-color code mapping [1]. (a) The color code can be obtained by encoding physical qubits of a pair of surface codes (blue and green) using $[\![4,2,2]\!]$ codes. (b) Depolarizing errors on the blue and green surface codes are mapped to the two-qubit bit-flip errors on the color code (i.e., logical X errors on the $[\![4,2,2]\!]$ codes). We emphasize that $\overline{X}_1 \equiv \overline{Z}_2$ and $\overline{Z}_1 \equiv \overline{X}_2$ with a Hadamard rotation under the surface code duplication. (c) Single-qubit depolarizing errors with their syndromes on the surface codes. (d) Stabilizers and logical operators of the $[\![4,2,2]\!]$ code defined on a square with qubits on its vertices. (e,f) For blue surface code (e), each physical qubit is encoded into the first logical qubit of a $[\![4,2,2]\!]$ code. The X (Z) checks of the blue surface code are mapped to blue (green) octagonal X (Z) checks of the color code. A similar mapping holds for the green surface code (f) after a transversal Hadamard rotation.

This section describes the mapping from the surface code to the color code. We refer the reader to Ref. [1] for a detailed illustration. Through this mapping, color code decoders for bit-flip errors can be adapted to decode the surface code against depolarizing errors. Furthermore, this mapping indicates that the restricted and correlated decoders for the color code can be derived from their counterparts for the surface code, as shown in Fig. A2.

The color code can be viewed as equivalent to two copies of the surface code [1–6]. The key insight is to construct the color code by encoding the physical qubits of a pair of overlapped surface codes (blue and green) using $[\![4,2,2]\!]$ codes (Fig. A1(a)). Each $[\![4,2,2]\!]$ code associated with the red square checks of the color code, encodes two corresponding physical data qubits of the two surface codes (Fig. A1(c)). Consequently, the checks of the two surface codes are mapped to octagonal checks of the color code, see Fig. A1(e,f).

Consider the mapping of the blue surface code as an example (the green one follows analogously). Each physical qubit of the blue code is encoded into the first logical qubit of a $[\![4,2,2]\!]$ code (red squares), and its corresponding physical X (Z) operator is then mapped to the logical operator $\overline{X}_1$ ($\overline{Z}_1$) of the $[\![4,2,2]\!]$ code. Note that the $[\![4,2,2]\!]$ codes in adjacent rows or columns are rotated by 90° to maintain the orientations of logical operators. Therefore, this mapping transforms the X (Z) checks of the surface code into the blue (green) octagonal X (Z) checks of the color code, as shown in Fig. A1(e).

Furthermore, we duplicate the surface code to support the full mapping, where the second green copy differs from the first blue one by a transversal Hadamard rotation. Under the duplication, with the Hadamard rotation, we have the following relations between pairs of logical operators of the $[\![4,2,2]\!]$ codes, namely $\overline{X}_1 \equiv \overline{Z}_2$ and $\overline{Z}_1 \equiv \overline{X}_2$. This ensures the syndrome correspondence in Fig. A1(b,c) such that all depolarizing errors on the surface codes now have a one-to-one mapping with a two-qubit bit-flip error on the color code. The resulting mapping from the blue surface code to the color code is as follows:

* Corresponding author (email: junjiewu@nudt.edu.cn, laolinglingrolls@gmail.com)

• A Z error that violates two adjacent X checks on the blue surface code (Fig. A1(c)(i)), is mapped to an $\overline{X}_2$ error that violates two adjacent blue checks on the color code (Fig. A1(b)(i)).

• An X error that violates two adjacent Z checks on the blue surface code (Fig. A1(c)(ii)), is mapped to an $\overline{X}_1$ error that violates two adjacent green checks on the color code, (Fig. A1(b)(ii)).

• A Y error that violates two adjacent X and Z checks on the blue surface code (Fig. A1(c)(iii)), is mapped to an $\overline{X}_1\overline{X}_2$ error that violates two adjacent blue and green checks on the color code (Fig. A1(b)(iii)).

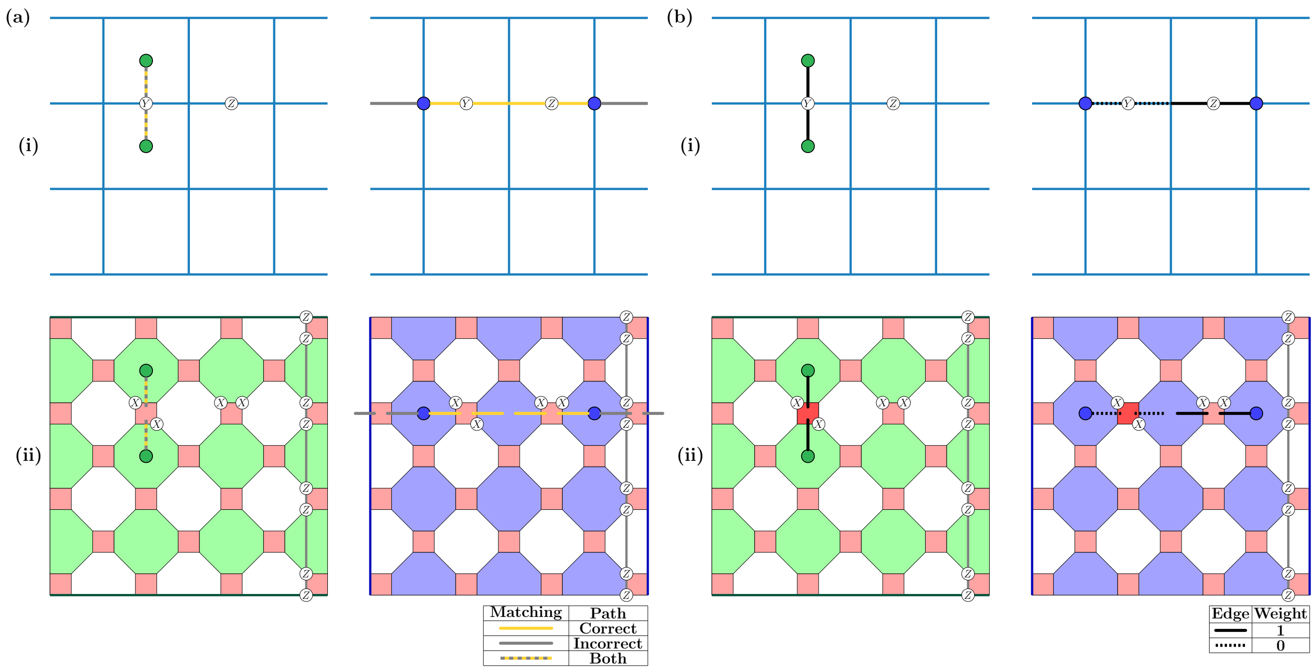

Figure A2 The restricted and correlated decoders for the color code can be derived from their surface code counterparts via the color-surface mapping. (a) The independent X/Z decoder (i) and the restricted decoder (ii) exhibit an analogous limitation: while decoding the degenerate weight-$O(d/2)$ error patterns (containing Y or diagonal errors), they overestimate the matching weight of the correct path, resulting in a success probability of only 1/2. (b) This issue is resolved by the correlated decoders for both codes (i, ii) by setting the weight of edges identified in the first matching to zero during the second matching. This ensures that the predicted error weight is consistent with the total matching weight, thus achieving more accurate decoding.

Appendix B Performance analysis at low error rates

In the regime of asymptotically low physical error rates, the logical error rate is mainly determined by the number of minimum-weight failure mechanisms:

$$P_{\text{fail}} \sim N_{\text{fail}}\, p^m (1-p)^{n-m} \sim N_{\text{fail}}\, p^m, \tag{B1}$$

where N_{fail} is the number of minimum-weight (m) error configurations leading to a logical failure. The low error-rate performance of the restricted and unified decoders has been thoroughly analyzed in Ref. [1] where the number of minimum-weight failure configurations for decoding the color code is given by

$$N_{\text{fail}}^{\text{res}} = \frac{M}{2} \sum_{k=0}^{\lfloor \frac{M}{2} \rfloor} \binom{M}{k} \binom{M-k}{k} 4^{M-k}, \tag{B2}$$

$$N_{\text{fail}}^{\text{uni}} = \frac{M}{2} \sum_{k=0}^{\lfloor \frac{M}{2} \rfloor} \binom{M}{k} \binom{M-k}{k} 2^k 4^{M-2k}, \tag{B3}$$

where M denotes the number of rows supporting $d/2$ red square plaquettes in the lattice, k is the number of red plaquettes raising a weight-2 error, and $M-2k$ is the number of weight-1 errors. The failure configurations of the restricted decoder consist of all weight-$d/2$ errors aligned along a single row, with the prefactor 1/2 accounting for the probability of the matching decoder correctly guessing the error. In contrast, the unified decoder excludes any error patterns containing a two-qubit diagonal error from these failure configurations.

Correlated decoder v1 achieves performance approximately comparable to that of the unified decoder for weight-$d/2$ errors. A small fraction of diagonal error patterns on the boundary rows (the first and last rows) is uncorrectable for v1 due to reduced check connectivity. To mitigate this, we slightly reduce the weights of the edges adjacent to the checks incident to the green boundary in $\mathcal{R}_{\mathbf{g}}$ lattice, thereby introducing a preference for boundary corrections in the correlated decoder. While this adjustment is heuristic, numerical evidence confirms that it effectively eliminates dominant boundary failure mechanisms without introducing new ones. We provide supporting evidence in Sec. Appendix E, including error configurations examples that can be corrected through this adjustment

(Fig. E1). After applying the adjustment, the remaining boundary failures are characterized by adjacent diagonal error pairs as shown in Fig. E3 of Appendix E, and quantified by N_{b}:

$$\begin{aligned} N_{\mathrm{b}} &= \frac{1}{2} \times 2 \sum_{i=1}^{\lfloor \frac{M}{4} \rfloor} \sum_{j=0}^{\lfloor \frac{M}{2}-2i \rfloor} \binom{M-i}{i} \binom{M-2i}{j} \binom{M-2i-j}{M-4i-2j} \times 4^i \times 2^j \times 4^{M-4i-2j} \\ &= \sum_{i=1}^{\lfloor \frac{M}{4} \rfloor} \sum_{j=0}^{\lfloor \frac{M}{2}-2i \rfloor} \binom{M-i}{i} \binom{M-2i}{j} \binom{M-2i-j}{M-4i-2j} \times 4^{M-3i-\frac{3}{2}j}, \end{aligned} \tag{B4}$$

where i is the number of adjacent diagonal error pairs, and j is the number of weight-2 errors located on the top/bottom edge of a square plaquette. The total number of minimum-weight failure configurations for the correlated decoder v1 is thus:

$$N_{\mathrm{fail}}^{\mathrm{v1}} = N_{\mathrm{fail}}^{\mathrm{uni}} + N_{\mathrm{b}}. \tag{B5}$$

The relative contribution $r = N_{\mathrm{b}}/N_{\mathrm{fail}}^{\mathrm{uni}}$ of additional boundary failure mechanisms is plotted as a function of code distance d in Fig. B1. Accordingly, the logical error rate of the correlated decoder exceeds that of the unified decoder by a factor of $1+r$. Given that r remains small for practical code distances, the performance of the correlated decoder closely approximates that of the unified decoder in the low error-rate regime.

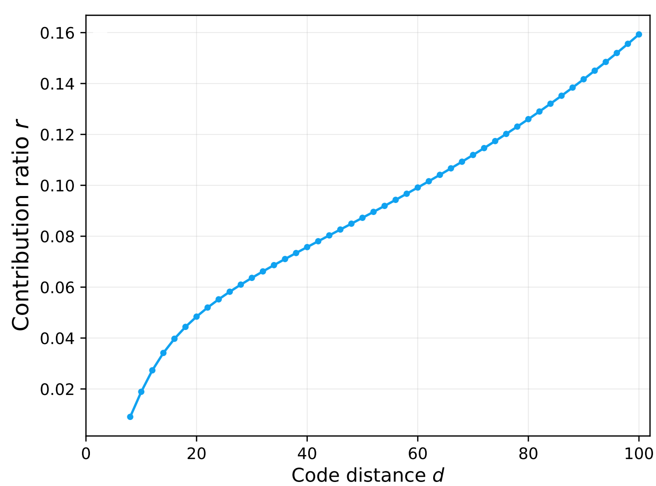

Figure B1 Relative contribution $r = N_{\mathrm{b}}/N_{\mathrm{fail}}^{\mathrm{uni}}$ of additional boundary failure mechanisms to the total failure configurations of the unified decoder, evaluated over code distance d ranging from 8 to 100.

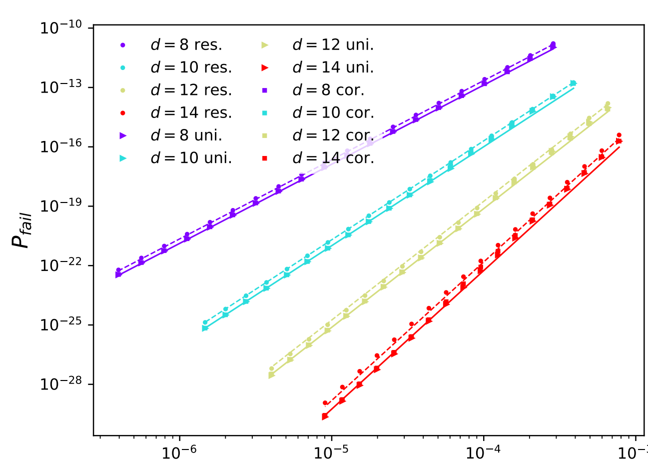

Figure B2 Logical failure rates at low physical error rates (logarithmic scale) for the restricted, unified and correlated v1 decoders (v2 achieves performance identical to the unified decoder) on the color code under bit-flip noise. Dashed and solid lines represent the analytical predictions for the restricted and unified decoders, respectively, based on path-counting methods [1].

Correlated decoder v2 achieves performance identical to that of the unified decoder, i.e., $N_{\rm fail}^{\rm v2} = N_{\rm fail}^{\rm uni}$, as verified by exhaustive enumeration of all weight-$d/2$ error configurations. To numerically evaluate the logical failure rates at low physical error rates, we use the rare-event splitting method introduced in Ref. [7], following the implementation in Ref. [1]. The results shown in Fig. B2 demonstrate good agreement with our analytical estimates.

Appendix C Generalized correlated decoder for circuit-level noise

We generalize our correlated decoder to accommodate circuit-level noise using *detector error model* (DEM) [8,9]. A DEM is defined by a set of *detectors* and *error mechanisms*. A detector is a linear combination of measurement outcomes whose product (or sum, in the corresponding binary representation) is deterministic in the absence of noise. An error mechanism is described as a 3-tuple $(q, \mathcal{D}, \mathcal{O})$, specifying the probability q that the error occurs, the set of detectors $\mathcal{D}$ and logical observables $\mathcal{O}$ it anti-commutes with.

We consider the logical Z measurement circuit for the color code of distance d. The circuit consists of an initialization stage, $r = d$ rounds of syndrome extraction, and a final measurement stage. All data qubits are initialized to $|0\rangle$ and measured in the Z basis at the end. For each syndrome extraction round, we adopt the simple conventional syndrome extraction circuit [10], which performs one round of Z stabilizer measurements followed by one round of X stabilizer measurements. In a Z (X) stabilizer measurement, ancilla qubits are first initialized to $|0\rangle$ ($|+\rangle$), followed by a sequence of CNOT gates between ancilla and data qubits, and concluded by a Z (X) basis measurement of the ancilla. While the specific CNOT schedule influences performance, we do not optimize it here and instead adopt the schedule (Fig. C1) specified in Ref. [10].

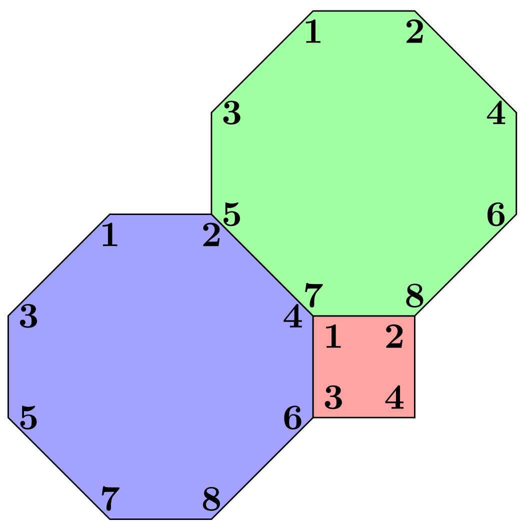

Figure C1 CNOT schedule for both X- and Z-type syndrome extraction circuits. The number at each vertex indicates the time slice that a CNOT gate is applied between the data qubit at that vertex and the ancilla qubit at the center of the face.

Consequently, the circuit yields $r+1$ rounds of Z-type detectors and $r-1$ rounds of X-type detectors, as the initial X measurement round completing the logical initialization yields random outcomes, and the final data-qubit measurements provide additional Z stabilizer information:

$$\begin{aligned} D_{f,Z}^{(t)} &:= \begin{cases} m_{f,Z}^{(1)} & \text{if } t = 1, \\ m_{f,Z}^{(t-1)} m_{f,Z}^{(t)} & \text{if } 2 \leqslant t \leqslant r, \\ m_{f,Z}^{(r)} \prod_{v \in f} \widetilde{m}_v & \text{if } t = r+1, \end{cases} \\ D_{f,X}^{(s)} &:= m_{f,X}^{(s-1)} m_{f,X}^{(s)} \qquad\quad 2 \leqslant s \leqslant r, \end{aligned} \tag{C1}$$

where $m_{f,Z}^{(i)}$ and $m_{f,X}^{(i)}$ are the ± 1 outcomes of Z and X stabilizer measurements on face f in round i, and $\widetilde{m}_v$ is the final ± 1 outcome of the data qubit at vertex v.

The detector error model (DEM) generated from the circuit cannot be decoded directly by PyMatching [11,12]. It requires decomposition such that all error mechanisms become edge-like. To enable this decomposition, each detector is pre-annotated with a basis and a color using an additional coordinate, following Chromobius [13]. For the logical Z measurement circuit, we decompose the full DEM $\mathcal{M}$ into the Z-type **rg**-color DEM $\mathcal{M}_{\mathbf{rg}}^{Z}$ and the Z-type **rb**-color DEM $\mathcal{M}_{\mathbf{rb}}^{Z}$. The decomposition proceeds analogously to Ref. [14]. Concretely, $\mathcal{M}_{\mathbf{rg}}^{Z}$ ($\mathcal{M}_{\mathbf{rb}}^{Z}$) is constructed by extracting from $\mathcal{M}$ all Z-type and also **rg**-color (**rb**-color) detectors, along with error mechanisms associated with them. Note that this process ignores X-Z correlations originating from depolarizing noise. Subsequently, the detector error model is compressed by merging error mechanisms that have an identical set of target detectors, updating their combined error probabilities accordingly.

We construct the two separate restricted decoding graphs from the DEMs $\mathcal{M}_{\mathbf{rg}}^{Z}$ and $\mathcal{M}_{\mathbf{rb}}^{Z}$. In the decoding graph of DEM, vertices represent detectors, and each error mechanism $(q, \mathcal{D}, \mathcal{O})$ corresponds to an edge connecting the detectors in $\mathcal{D}$ with an edge weight of $\log[(1-q)/q]$. The two decoding graphs illustrated in Fig. C2(a)(ii) are analogous to the phenomenological-noise decoding graph. However, they contain additional edges that correspond to two-qubit depolarizing errors following CNOT gates within the syndrome

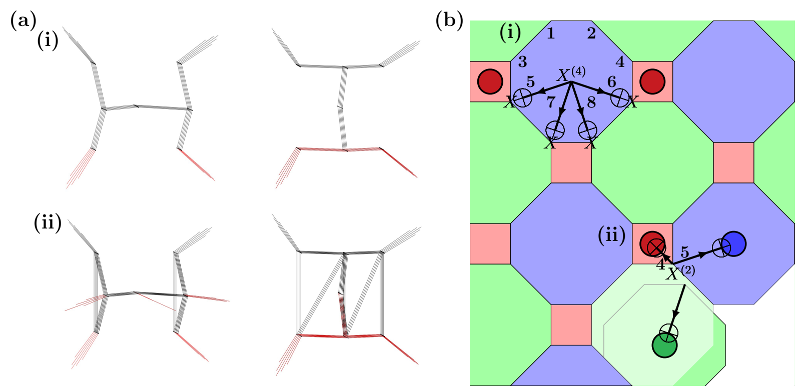

Figure C2 (a) (ii) DEM $\mathcal{M}^Z_{\mathbf{rg}}$ (left) and $\mathcal{M}^Z_{\mathbf{rb}}$ (right) for $d = 4$ generated by Stim. Removing the two-qubit depolarizing noise channel from circuit yields (i) which has the same structure as the phenomenological-noise decoding graph (Fig. D2). The additional error mechanisms from the two-qubit depolarizing noise complicate the DEM and reduce the code distance. (b) Examples of these complex error mechanisms. (i) An $X^{(4)}$ error (superscript indicates the time slice of CNOT gate the error follows) on an X ancilla qubit during X syndrome extraction propagates through subsequent CNOT gates, creating a syndrome of two red detectors in the following Z syndrome extraction. (ii) An $X^{(2)}$ error on a data qubit violates the red and blue detectors in the current Z syndrome extraction round, while triggering the green detector in the next round.

extraction circuit, which significantly reduce the circuit-level code distance. This reduction occurs because the simple syndrome extraction circuit is not fault-tolerant; errors can propagate through CNOT gates, giving rise to more complex error mechanisms such as hook errors [15] (see examples in Fig. C2(b)). While addressing these errors—for example, by optimizing the CNOT schedule or using flag qubits [16, 17]—is an important direction for improving decoding performance, the design and evaluation of such methods fall outside the scope of the present work. After constructing the two restricted decoding graphs, we can apply the correlated decoding procedure under phenomenological noise while limiting the marking and reweighting operations to the subset of edges in Fig. C2(a)(i).

Appendix D Additional numerical results

Appendix D.1 Decoding time analysis

The decoding time benchmarks are shown in Fig. D1. The results are broadly consistent with the analysis in the main text.

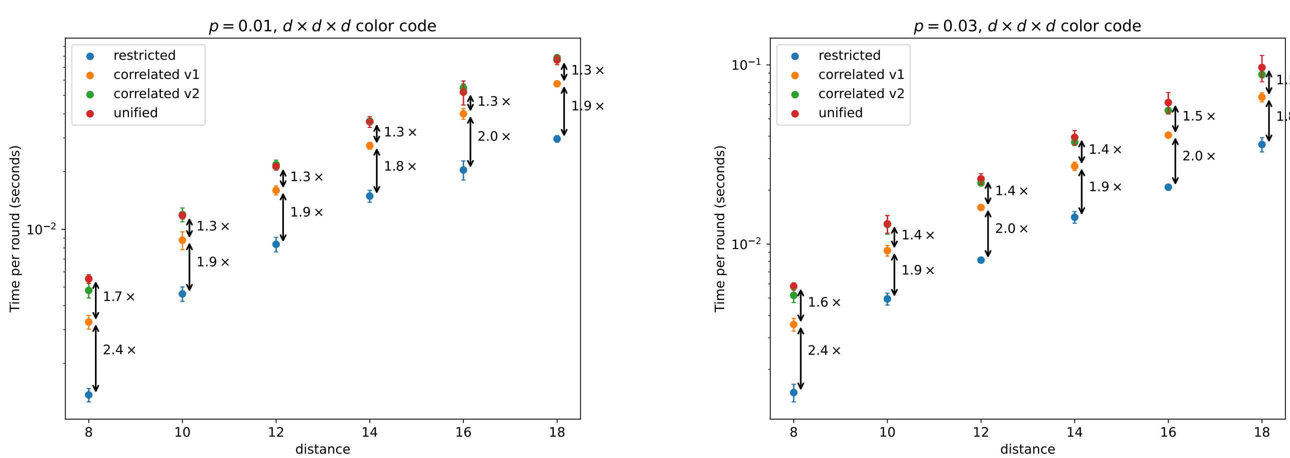

Figure D1 Comparison of per-round decoding time for the three decoders under phenomenological noise at $p = 0.01$ and $p = 0.03$.

Appendix D.2 Phenomenological noise threshold

The correlated decoding procedure is adapted to the phenomenological noise model by applying the same process to the space-time matching graphs, as shown in Fig. D2. The phenomenological noise thresholds are shown in Fig. D3.

Appendix D.3 Circuit-level noise performance

The circuit-level noise performance is shown in Fig. D4.

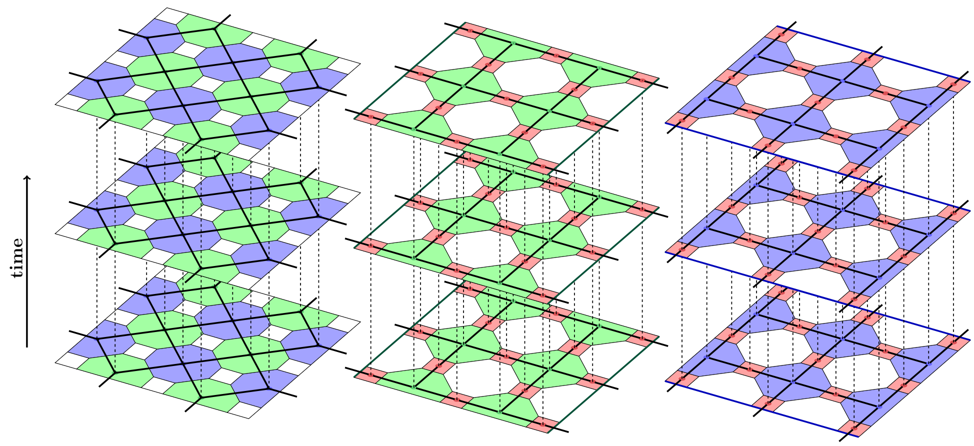

Figure D2 The space-time matching graphs of three restricted lattices for $r = 3$ rounds under the phenomenological noise model. Time progresses upward from the bottom, with each horizontal plane corresponding to a round of stabilizer measurements. The vertical dashed edges represent space-time locations where measurement errors may occur.

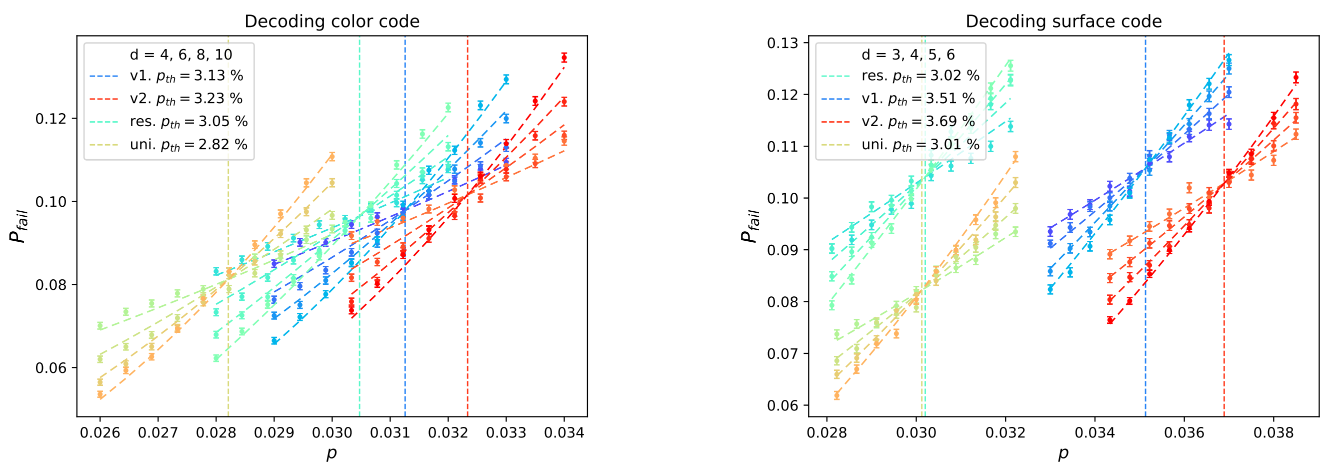

Figure D3 Threshold comparison of the restricted, unified, and correlated decoders for the color code and the surface code under the phenomenological noise model. The number of stabilizer measurement rounds r is set to the distance d.

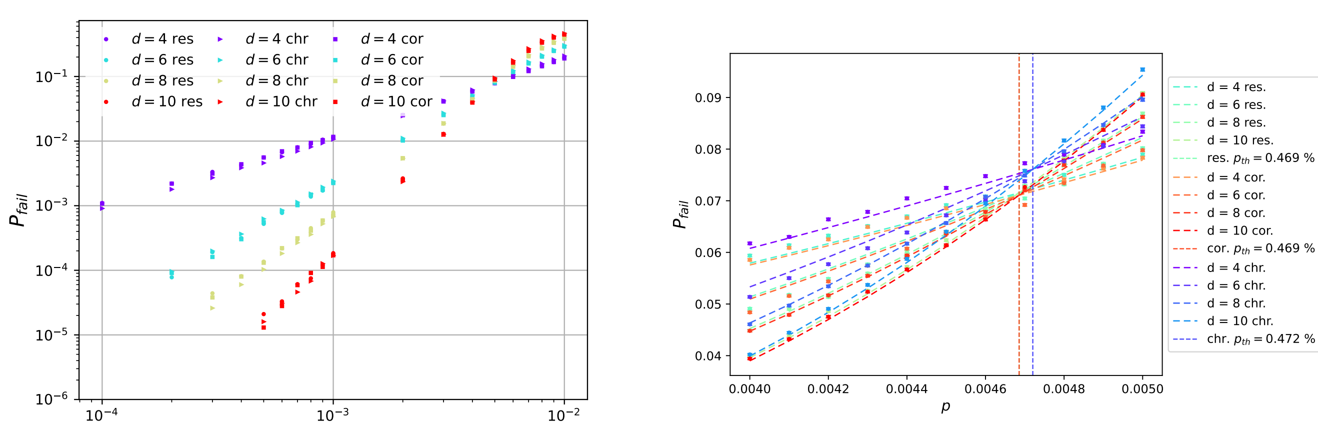

Figure D4 Comparison of the three matching-based decoders (the restricted, correlated and Chromobius decoders) under circuit-level noise. **Left:** Logical error rate as a function of physical error rate. **Right:** Rescaled logical error rate near threshold, highlighting the relative performance.

Appendix E Uncorrectable weight-$d/2$ diagonal error patterns for correlated decoder v1

The correlated decoder v1 successfully corrects the degenerate weight-$d/2$ error patterns involving diagonal errors within the middle rows of the lattice. Adjacent diagonal errors (Fig. E2) in the bulk have a theoretical 1/4 failure probability for v1, but the deterministic preference of the decoder avoids this in practice. However, a subset of such errors located on the boundary rows (i.e., the first and last rows) becomes more difficult to correct due to the reduced check connectivity. Here we provide a detailed analysis of these boundary errors.

To support our analysis, we introduce the following notation. Minimum-weight failure configurations along a row of $M = d/2$ red squares consist of four error types per square: Diagonal errors (2 configurations), Edge errors (2 configurations), Single errors (4 configurations), and No error (1 configuration), denoted by their initial letters as illustrated in the top-left of Fig.E1. An error pattern is defined as a multiset $\{e_1, e_2, \ldots, e_{d/2}\}$ where element order is irrelevant and each $e_i \in \{\text{D, E, S, N}\}$. For example, the pattern {D, S, S, N} corresponds to one diagonal-error square, two single-error squares, and one no-error square in a row. The number of such configurations is given by $\binom{4}{1}\binom{3}{1} \times 2 \times 4^2$.

By modifying the weight w_b of the edges connected to the top and bottom red checks in the $\mathcal{R}_\mathbf{b}$ lattice from 1 to 0.999, the number of additional boundary failures is dramatically reduced without introducing new minimum-weight failures. As summarized in Tab. E1, the simulated failure counts N (before adjustment) and N' (after adjustment) show significant reductions for specific error patterns. Fig. E1 shows correctable boundary failure examples by this adjustment.

The remaining boundary failures after adjustment are characterized by adjacent diagonal error pairs and quantified by N_b in Eq. B4. Table E1 also provides theoretical estimates for these residual errors across $d = 6$ to 14, which align closely with the simulated values N'. Representative examples of the corresponding boundary failure configurations are shown in Fig. E3. The correlated decoder v2 improves the handling of adjacent diagonal error patterns and boundary error patterns that v1 may fail to correct, as shown in Fig. E2.

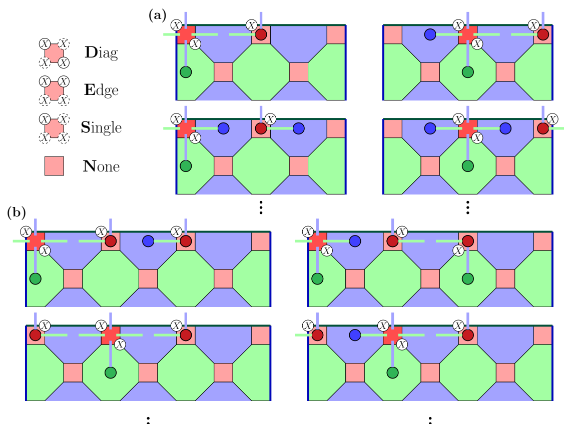

Figure E1 Examples of the error configurations that become correctable after modifying w_b to 0.999. Blue and green matchings indicate correct matchings in the $\mathcal{R}_\mathbf{g}$ and $\mathcal{R}_\mathbf{b}$ lattices, respectively.

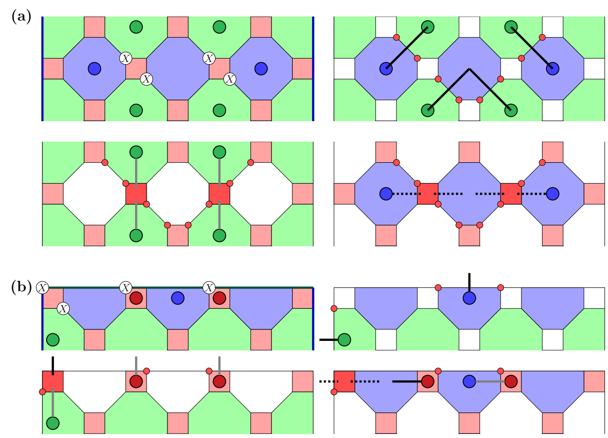

Figure E2 Examples of improved $O(d/2)$ diagonal error patterns of correlated decoder v2 over v1. (a) Adjacent diagonal error patterns. (b) Boundary error patterns.

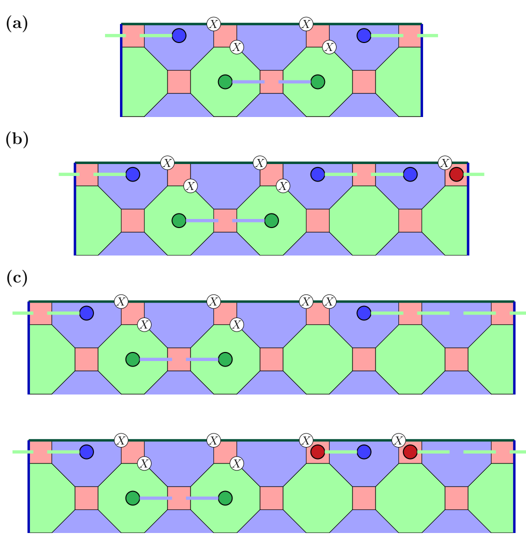

Figure E3 Examples of remaining failure configurations consisting of adjacent diagonal error pairs. Blue and green matchings indicate failed matchings in the $\mathcal{R}_\mathbf{g}$ and $\mathcal{R}_\mathbf{b}$ lattices, respectively, occurring with probability 1/2.

d	Pattern	N	N'	$N_\mathrm{b}(i,j)$
6	{D,S,N}	6	0	0
8	{D,S,S,N}	72	0	0
	{D,D,N,N}	4	4	6
10	{D,D,S,N,N}	88	88	96
	{D,E,S,N,N}	92	0	0
	{D,S,S,S,N}	584	0	0
12	{D,D,E,N,N,N}	64	64	80
	{D,D,S,S,N,N}	1036	896	960
	{D,E,S,S,N,N}	1676	0	0
	{D,S,S,S,S,N}	3888	0	0
14	{D,D,D,S,N,N,N}	288	0	0
	{D,D,E,S,N,N,N}	1888	1888	1920
	{D,E,E,S,N,N,N}	864	0	0
	{D,D,S,S,S,N,N}	10040	7360	7680
	{D,E,S,S,S,N,N}	19472	0	0
	{D,S,S,S,S,S,N}	23184	0	0

Table E1 Enumeration for extra boundary errors in a single row from $d = 6$ to 14. N and N' represent simulated failure counts with $w_b = 1$ and $w_b = 0.999$. $N_\mathrm{b}(i,j)$ is the analytical estimate of N' from Eq. B4 for specific values of i and j within a boundary row. Minor deviations between simulation and theory may arise from the deterministic behavior and preference of the decoder.

References

1 Benhemou A, Sahay K, Lao L, et al. Minimising surface-code failures using a color-code decoder. Quantum, 2025, 9: 1632
2 Yoshida B. Classification of quantum phases and topology of logical operators in an exactly solved model of quantum codes. Annals of Physics, 2011, 326: 15–95
3 Bombin H, Duclos-Cianci G, Poulin D. Universal topological phase of two-dimensional stabilizer codes. New Journal of Physics, 2012, 14: 073048
4 Bhagoji A, Sarvepalli P. Equivalence of 2d color codes (without translational symmetry) to surface codes. In: Proceedings of 2015 IEEE International Symposium on Information Theory (ISIT), 2015. 1109
5 Kubica A, Yoshida B, Pastawski F. Unfolding the color code. New Journal of Physics, 2015, 17: 083026
6 Criger B, Terhal B. Noise thresholds for the [[4, 2, 2]]-concatenated toric code. arXiv:1604.04062, 2016
7 Bravyi S, Vargo A. Simulation of rare events in quantum error correction. Physical Review A, 2013, 88: 062308
8 Gidney C. Stim: a fast stabilizer circuit simulator. Quantum, 2021, 5: 497
9 Derks P J H, Townsend-Teague A, Burchards A G, et al. Designing fault-tolerant circuits using detector error models. Quantum, 2025, 9: 1905
10 Landahl A J, Anderson J T, Rice P R. Fault-tolerant quantum computing with color codes. arXiv:1108.5738, 2011
11 Higgott O. Pymatching: A python package for decoding quantum codes with minimum-weight perfect matching. ACM Transactions on Quantum Computing, 2022, 3: 1–16
12 Higgott O, Gidney C. Sparse blossom: correcting a million errors per core second with minimum-weight matching. Quantum, 2025, 9: 1600
13 Gidney C, Jones C. New circuits and an open source decoder for the color code. arXiv:2312.08813, 2023
14 Lee S H, Li A, Bartlett S D. Color code decoder with improved scaling for correcting circuit-level noise. Quantum, 2025, 9: 1609
15 Dennis E, Kitaev A, Landahl A, et al. Topological quantum memory. Journal of Mathematical Physics, 2002, 43: 4452–4505
16 Takada Y, Fujii K. Improving threshold for fault-tolerant color-code quantum computing by flagged weight optimization. PRX Quantum, 2024, 5: 030352
17 Chamberland C, Kubica A, Yoder T J, et al. Triangular color codes on trivalent graphs with flag qubits. New Journal of Physics, 2020, 22: 023019